



Visible-light active black TiO₂-Ag/TiO_x particles

Kakeru Fujiwara^a, Yiannis Deligiannakis^{a,b},
Charalambos G. Skoutelis^b, Sotiris E. Pratsinis^{a,*}

^a Particle Technology Laboratory, Institute of Process Engineering, Department of Mechanical and Process Engineering, ETH Zurich, Sonneggstrasse 3, CH-8092 Zurich, Switzerland

^b Laboratory of Physical Chemistry of Materials and Environment, Department of Environmental and Natural Resources Management, University of Patras, Seferi 2, 30100 Agrinio, Greece

ARTICLE INFO

Article history:

Received 24 October 2013

Received in revised form 27 January 2014

Accepted 30 January 2014

Available online 7 February 2014

Keywords:

Nanosilver

Titanium oxide

Photocatalyst

Flame synthesis

Strong metal–support interaction

ABSTRACT

Visible-light active materials are sought in photocatalysis and solar energy utilization. Here a material architecture active under visible-light and comprising of titanium suboxide (e.g. Ti₄O₇, Ti₃O₅) layers onto nanosilver on nanostructured TiO₂ is formed by flame aerosol technology. Abundant combustion intermediates present during flame synthesis of these materials partially reduce TiO₂ and induce strong metal–support interactions (SMSI) resulting in crystalline Ti-suboxides as determined by X-ray diffraction. The growth of such suboxides can be controlled through their flame spray synthesis conditions allowing for tuning the light absorption intensity in the visible spectrum. The as-prepared Ti-suboxides are stable upon annealing in air, at least, up to 350 °C for 2 h. Their presence on the Ag/TiO₂ particle surface and efficiency in generating photoinduced charge separation under visible light is demonstrated by electron paramagnetic resonance spectroscopy. Under visible light ($\lambda > 400$ nm), these nanoparticles exhibit strong photo-reduction of cationic species (Cr⁶⁺) and photo-oxidation of organics (methylene blue).

© 2014 Elsevier B.V. All rights reserved.

1. Introduction

Recently, a so-called “black” titania with remarkable activity under visible light ($\lambda > 400$ nm) has been proposed for efficient solar energy utilization [1,2]; the photoactivity occurs preferentially on the surface of these particles. This “black” titania consists of either a crystalline stoichiometric TiO₂ core and a disordered reduced self-doped shell [1] or by a crystalline reduced TiO₂ core (with oxygen vacancies) surrounded by a nearly stoichiometric amorphous shell [2]. Such a titanium suboxide with TiO₂ particles can be produced by laser irradiation [3] or by reduction under high pressure [1] or temperature [2] with H₂, organic solvents [4], NaBH₄ [5] or CaH₂ [6] for several hours/days. In addition, binary TiO₂–Ti₂O₃ is formed under prolonged UV irradiation (several hours) of sol–gel-made TiO₂ [7]. The improved visible-light photoresponse of Ti suboxides involves the modulation of the energy levels of the semiconductor: Ti³⁺ defects that enhance visible-light photoactivity by introducing band-gap energy states [2,4]. In addition, the distorted titanium suboxide shell on TiO₂ creates an additional energy “tail” from the valence band into the band gap [1,2]. Thus, the engineering of Ti-suboxide phase on crystalline TiO₂ opens new opportunities for

visible-light active TiO₂. Most of the above synthesis techniques, however, require extreme processing conditions offering limited control of the suboxide phase formation so their applicability to mass production is not straightforward.

On the other hand, TiO₂ and specific metals (e.g. Pt, Pd, Ni or Ag) exhibit an abnormal interaction [8–11], the so-called strong metal–support interaction (SMSI). Under H₂ reduction at high temperatures, the TiO₂ surface is reduced. The so-formed Ti³⁺ can either interact with the metal phase, thereby forming weak covalent bonds [9] or receive electrons from it [12]. Then the Ti³⁺ can diffuse to the surface of noble metal or TiO₂ [7] and surround them, thereby forming titanium suboxide [8,9]. Indeed, the formation of Ti³⁺ on the Pt–TiO₂ surface by SMSIs has been observed with X-ray photoelectron spectroscopy [13]. Such a distorted titanium suboxide has been seen also by transmission electron microscopy (TEM) in Pd–TiO₂ [14]. The chemical structure of titanium suboxide depends on reducing conditions. Above 600 °C in H₂, Ti₄O₇ can be formed [15] whereas further reduction to Ti₃O₅ may require a radical structure [9] reorganization.

Here “black” composite TiO₂ nanoparticles (NPs) consisting of TiO₂, titanium suboxide and nanosilver are prepared in one-step by a continuous gas-phase method, flame spray pyrolysis (FSP) [16] that is scalable to kg/h [17]: titanium and silver precursors in flammable solvents are sprayed and dispersed by O₂ in fine mists that are combusted resulting in TiO_x onto nanosilver on

* Corresponding author.

E-mail address: pratsinis@ptl.mavt.ethz.ch (S.E. Pratsinis).

predominantly anatase TiO_2 NPs. This flame aerosol technology produces rapidly in one step high purity materials (e.g. optical fibers) without liquid byproducts and any post-processing. As a result, it is used in large scale manufacture (tons/h) of carbon black, pigmentary titania and fumed oxides [18]. The structural profiles of these TiO_2 -Ag/ TiO_x NPs are investigated by TEM, diffuse reflectance spectroscopy and X-ray diffraction (XRD). Their photoactivity is monitored by electron paramagnetic resonance (EPR) spectroscopy. Finally, the photocatalytic performance of the NPs with respect to Cr^{6+} and methylene blue (MB) degradation are examined under visible light ($\lambda > 400 \text{ nm}$).

2. Materials and methods

2.1. Catalyst preparation and characterization

TiO_2 -titanium suboxide (“black” TiO_2) NPs loaded with 10 or 20 wt.% of Ag (10Ag/ TiO_2 or 20Ag/ TiO_2) were prepared by single step FSP and collected on glass-fiber filters [19]. Silver acetate (Aldrich, purity > 99%) and titanium isopropoxide (TTIP, Aldrich, purity > 97%) were used as silver and titanium precursors, respectively. The total precursor (TTIP and silver acetate) concentration in a 1:1 mixture of 2-ethylhexanoic acid (Aldrich, purity > 99%) and acetonitrile (Aldrich, purity > 99.5%) was 0.16 M. The precursor solution was fed through the FSP nozzle at $X = 3$ or 8 mL/min, dispersed to a fine spray by $Y = 5 \text{ L/min}$ oxygen (Pan Gas, purity > 99%), hereafter referred to as the FSP X/Y feed ratio, and combusted to produce high-purity NPs. Additionally, 20Ag/ TiO_2 NPs were prepared at $X/Y = 8/5$ with additional 20 L/min sheath O_2 flowing through an annulus surrounding that for O_2 dispersion [19].

Scanning transmission electron microscopy (STEM) images were recorded with a high-angle annular dark-field detector (Hitachi, HD 2700-Cs, 200 kV, point resolution $\sim 1.4 \text{ \AA}$). The concentration of each element at selected spots in the STEM images was determined by energy-dispersive X-ray (EDX) analysis (EDAX detector, Genesis, Hitachi). High-resolution TEM was performed with a Tecnai F30-ST microscope (FEI, 300 kV, point resolution $\sim 2 \text{ \AA}$). As-prepared particles were dispersed in ethanol and deposited onto a perforated carbon foil supported on a copper grid.

XRD patterns were obtained by a Bruker AXS D8 Advance diffractometer ($\text{Cu K}\alpha$, 40 kV, 40 mA) at $2\theta = 20\text{--}50^\circ$ with a step size of 0.03° . The exposure time for each step was 2.5 s for high-quality XRD patterns. Crystalline mass fractions were calculated from the integral intensities of each peak (OriginPro, 8.6). A background signal corresponding to amorphous phases was corrected in the spectra by software (EVA). As the Ti_4O_7 peaks at 28.5° and 29.5° overlap, its integral intensity was set to be half the peak area at 29.5° . Raman spectroscopy was performed (Renishaw InVia Reflex Raman) with a 514 nm diode (Ar-ion laser, 25 mW) laser as excitation source focused with a microscope (Leica, magnification $50\times$). The samples were pressed into tablets and placed on a glass plate. The spectra were recorded for 10 s with 20 accumulations to obtain sufficient signal-to-noise ratio with a CCD camera after being diffracted by a prism (1800 lines per millimeter) using 3.75 mW laser energy.

2.2. Characterization of visible light activity and photocatalysis

Diffuse-reflectance spectra of the catalysts were measured by a Varian Cary 500 UV–vis spectrophotometer equipped with an integrating sphere. EPR spectra were recorded at 77 K with a Bruker ER200D spectrometer equipped with an Agilent 5310A frequency counter. For each experiment, 10 mg of NPs are placed inside a quartz EPR tube (Suprasil, Willmad Glass) with an outer diameter of 3 mm. The EPR signals presented herein were recorded at

9.49 GHz, using a modulation amplitude of 4 G, a field modulation of 100 kHz and 4 mW microwave power. Adequate signal-to-noise ratios were obtained with 10 scans. A solar-light-simulating Xe light source (Oriel model 66929, 450 W) equipped with a water IR filter was used to investigate photogeneration of electrons and holes. Visible-light illumination ($\lambda > 400 \text{ nm}$) was performed using a longpass 400 nm filter (Edmund Optics 85754). The same light source was used for photocatalytic experiments.

Photocatalytic degradation of Cr^{6+} and methylene blue (MB) was performed in a Pyrex glass container. For Cr^{6+} degradation, 9 mg of NPs was dispersed in 90 mL of Milli-Q water ($C_{\text{catalyst}} = 100 \text{ mg/L}$) in a water-bath sonicator. The solution pH was adjusted to 3.5 with HNO_3 . $\text{K}_2\text{Cr}_2\text{O}_7$ (Aldrich) was added at an initial concentration of $C_{\text{Cr}} = 0.5 \text{ mM}$. Salicylic acid (SA) (Aldrich) was added at a concentration of $C_{\text{SA}} = 5 \text{ mM}$ to optimize the photocatalytic kinetics [20]. For MB degradation, 22.5 mg of NPs were dispersed in 90 mL of Milli-Q water ($C_{\text{catalyst}} = 250 \text{ mg/L}$) in a water-bath sonicator. Methylene blue (Aldrich) was added at an initial concentration of $C_{\text{MB}} = 0.01 \text{ mM}$. The solution pH was adjusted to 9.0 with NaOH [21]. The solutions were mixed with the appropriate amount of photocatalyst and magnetically stirred before and during the illumination. The suspensions were kept in the dark for 30 min prior to illumination to reach adsorption equilibrium on the semiconductor surface. As the reaction progressed, samples were withdrawn from the reactor at specific time intervals. The MB suspension was centrifuged for 15 min at 4000 rpm using a Hettich Universal 16A centrifuge for further analysis. The MB decolorization was determined by monitoring the change in optical absorption at 660 nm [21] using a Perkin Elmer Lambda 35 double-beam UV–vis spectrophotometer. The Cr^{6+} ions in each solution were determined by the diphenylcarbazide method [20] using the UV–vis spectrophotometer.

3. Results and discussion

3.1. Catalyst properties

By controlling the FSP feed ratio of the Ti/Ag precursor solution flow to that of dispersion O_2 , appropriate conditions for particle synthesis are selected [19]. Fig. 1a shows images of P25 (commercial TiO_2) and FSP-made TiO_2 NPs loaded with Ag (10 or 20 wt.% of composite Ag/ TiO_2 particles) prepared at X/Y feed ratio of 3/5 and 8/5. A high Ag loading (e.g. 20 wt.%) and a high FSP feed ratio (e.g. 8/5) resulted in the darkest particles (Fig. 1a). These dark colors are similar to H_2 -reduced TiO_2 [2] and do not come from incomplete combustion products remaining on the particle surface. Thermogravimetric analysis showed <2% of organic loading and EPR showed zero carbon-based radicals. The color changes correspond to formation of TiO_x which exhibits an absorption band in the visible range [22].

Fig. 1b shows a STEM image of the 20Ag/ TiO_2 NPs prepared at $X/Y = 8/5$ with EDX analysis at different points (c–e). The darker and lighter parts in the STEM image correspond to titanium oxide and silver, respectively, (e.g. points c and d). At point (c), Ti/O are dominant and Ag hardly appears as its signal is less than that of the Cu support (not shown here). At point (d), the titanium peak practically does not appear, indicating predominantly Ag NP. On the other hand, both Ag and titanium are detected at the weakly bright point (e) indicating that Ag NPs might be embedded or coated (fully or partially) by TiO_x .

Fig. 1f shows a TEM image of the 20Ag/ TiO_2 NPs prepared at $X/Y = 8/5$ with its higher resolution and magnification at Fig. 1g. In contrast to STEM (Fig. 1b), the lighter and darker parts correspond to titanium oxide and silver, respectively. This image reveals that the darker Ag NPs are embedded and fully or partially coated or

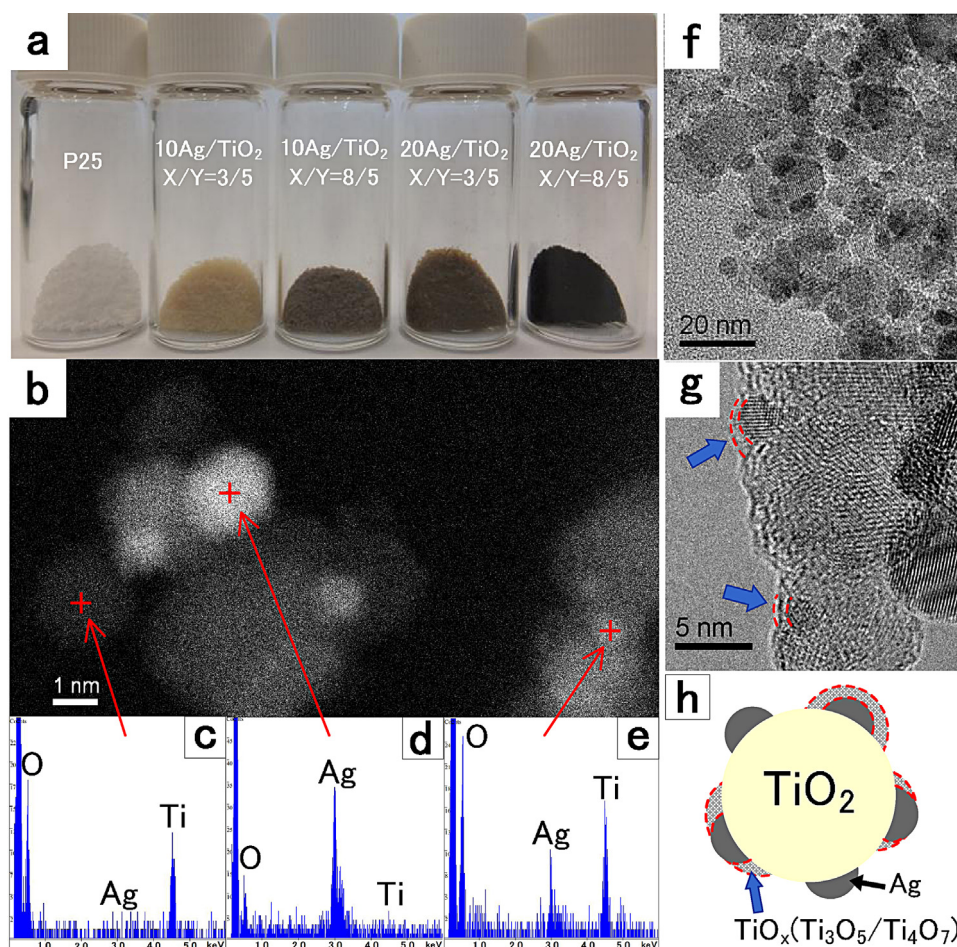


Fig. 1. (a) Commercial (P25) and FSP-made TiO_2 loaded with Ag (10 or 20 wt.%) prepared at low ($X/Y = 3/5$) and high ($8/5$) temperature and Ti concentration. (b) STEM image and EDX analysis of $20\text{Ag}/\text{TiO}_2$ made at $X/Y = 3/5$. Positions (c–e) for EDX analysis are marked in the STEM image. (f) TEM image of $20\text{Ag}/\text{TiO}_2$ made at $X/Y = 8/5$ with selected (g) high-resolution images. The blue arrows and red broken lines indicate disordered titanium oxide onto nanosilver and TiO_2 . (e) Schematic of titanium suboxide onto nanosilver and TiO_2 created by strong metal–support interactions (SMSI). (For interpretation of the references to colour in this figure legend, the reader is referred to the web version of the article.)

decorated (Fig. 1g) by layered titanium oxide (indicated by broken red lines). Similar morphologies have been observed with strongly interacting Co [23] and Pt [24] nanostructures on TiO_2 produced by H_2 reduction at high temperatures. This morphology indicates SMSI that result in embedding or partial encapsulation or coating of noble metal clusters by titanium suboxides [8,14,23] indicated here by blue arrows in Fig. 1g similar to Pt– CeO_2 made by SMSI [25]. Fig. 1h shows schematically such distorted Ti-suboxide onto Ag/ TiO_2 partially encapsulating and exposing the nanosilver.

Silver does not form independently SMSI because it cannot dissociate H_2 and generate Ti^{3+} states; Ag, however, can create SMSIs in the presence of Pt, which facilitates hydrogen dissociation [10]. Here, abundant intermediate combustion products are present during flame synthesis of TiO_2 that can reduce it similarly to dissociated hydrogen [4] and induce SMSI on Ti–Ag that facilitate crystallization of titanium suboxides and/or prevent complete oxidation of the newly formed titanium suboxides.

Fig. 2a shows the XRD patterns of 10 and $20\text{Ag}/\text{TiO}_2$ NPs prepared at $X/Y = 3/5$ or $8/5$, respectively. A higher FSP feed ratio (e.g. $X/Y = 8/5$) results in stronger and sharper peaks indicating larger crystals. Increasing the X/Y ratio increases particle mass concentration and residence time at high temperatures that lead to larger particles by enhanced coagulation and sintering [26]. The peaks at 25.5° and 48° correspond to anatase TiO_2 (diamonds) that are dominant in all particles. Only particles prepared at $X/Y = 8/5$ (blue, black

and purple spectra) contain a small peak around 27.5° corresponding to rutile (circles). The Ag^0 peaks (squares) at 44° are distorted more than those of flame-made Ag^0 NPs supported [10] on SiO_2 indicating the SMSI between Ag and TiO_2 here.

Most interestingly, titanium suboxides were resolved by XRD: Ti_3O_5 (down triangles) at 33° and Ti_4O_7 (up triangles) at 28.5° and 29.5° in Fig. 2a. Note, however, that the Ti_4O_7 peaks might correspond also to other suboxides, especially $\text{Ti}_x\text{O}_{2x-1}$ (e.g. Ti_5O_9) that have similar connectivity and diffraction features [27]. Analogous features, however, have been reported [6,28] for Ti_3O_5 and Ti_4O_7 formed by SMSI [9,15], supporting the present assignment of the 28.5° and 29.5° peaks to Ti_4O_7 . Here, the suboxide peaks are broad, indicating small crystals and/or low crystallinity, consistent with their layered morphology (Fig. 1c, d). The peak intensities increased with increasing Ag loading and FSP feed ratio (reducing flame conditions) corresponding to the darkening of these particles (Fig. 1a).

Fig. 2b shows the XRD-mass fractions of anatase (red diamonds), rutile (black circles), Ag^0 (orange squares), Ti_3O_5 (blue down triangles), and Ti_4O_7 (green up triangles) phases for the particles in Fig. 2a. The mass fraction of anatase decreased with increased nominal mass fraction of Ag (from 10% to 20%) and reducing flame conditions (X/Y from $3/5$ to $8/5$). This was accompanied by increases in the mass fractions of rutile, Ti_3O_5 and Ti_4O_7 . Highly reducing conditions result in SMSIs of Pd [14] and Pt [15] with TiO_2 that

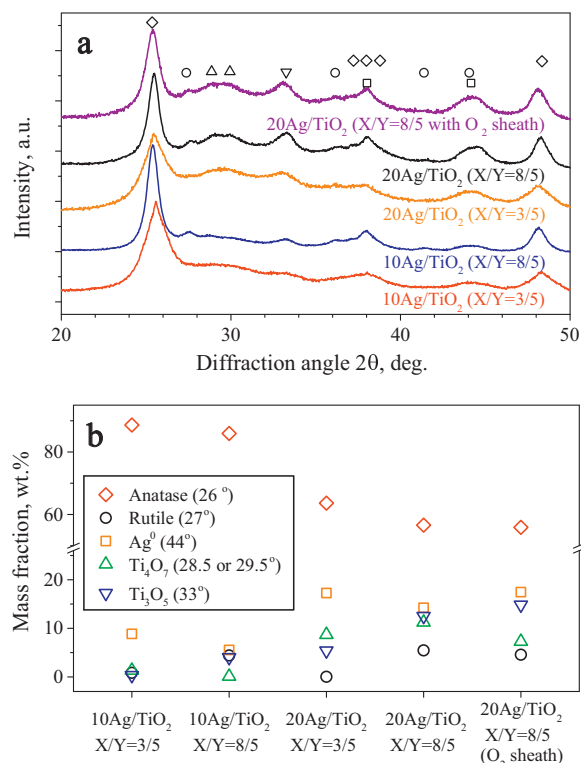


Fig. 2. (a) XRD patterns and (b) mass fractions of 10Ag/TiO₂ and 20Ag/TiO₂ prepared at FSP feed X/Y=3/5 and 8/5 and 20Ag/TiO₂ prepared at X/Y=8/5 with 20 L/min of sheath O₂. Diffraction patterns are marked for TiO₂ anatase (diamonds) and rutile (circles) as well as for Ag⁰ (squares), Ti₄O₇ (up triangles) and Ti₃O₅ (down triangles).

lead to formation of Ti₄O₇. For further reduction to Ti₃O₅, a radical reorganization of the structure may be required [9].

The Ag⁰ mass fraction in all particles was slightly lower than its nominal value (10 or 20 wt.%) and decreased with reducing flame conditions similarly to anatase mass fraction. This reduction in Ag⁰ mass fraction could be attributed to the interaction of Ti³⁺ with isolated Ag atoms created by electron transfer from Ag to titanium [12]. The use of additional O₂ as a sheath gas during FSP made the flame more oxidative and affected suboxide formation (Fig. 2a, purple spectrum). The mass fraction of Ti₄O₇ decreased whereas that of Ti₃O₅ slightly increased compared to those in the absence of sheath O₂ (Fig. 2a, black spectrum) as shown in Fig. 2b. The use of O₂ sheath during FSP increases the conversion of the precursor solution [17], flame temperature and subsequently the high temperature residence time of the particles [26].

Fig. 3 shows (a) the XRD patterns and (b) mass fractions of 20Ag/TiO₂ prepared at X/Y=8/5 (black spectrum) and annealed at 350 (pink spectrum) and 550 °C (brown spectrum) in air for 2 h. These patterns indicate that the titanium suboxide phases are stable, at least, up to 350 °C but transformed to rutile at 550 °C [29] with remnant Ti₃O₅ and Ti₄O₇ [28] as shown quantitatively in Fig. 3b. Moreover, during this annealing, isolated Ag atoms [12] with Ti³⁺ sinter with exposed Ag particles (by the decomposition of suboxides) increasing the Ag mass fraction back to its nominal 20%. This provides further indication to promotion of suboxide formation during FSP by the presence of silver.

Fig. 4 shows Raman spectra of “black” TiO₂ NPs loaded with Ag (10 or 20 wt.%) and made at X/Y=3/5 or 8/5. Most notably, no Raman peak for silver was detected in contrast to FSP made 95Ag/SiO₂ particles [30] (dashed line). The Raman spectra of all Ag/TiO₂ show new peaks at 246 and 361 cm^{−1} and a stronger one at 199 cm^{−1} than that of commercial TiO₂, P25. Analogous features have been observed in the Raman spectra of “black” TiO₂ [1]. However, some peaks (294,

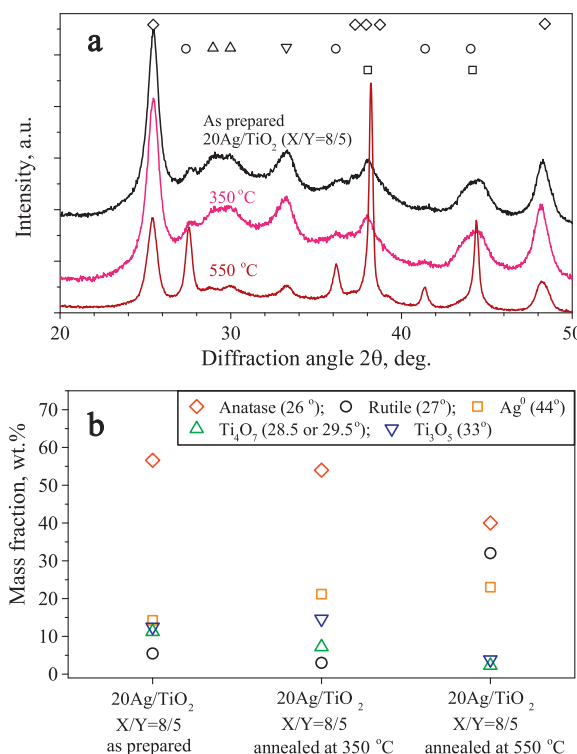


Fig. 3. (a) XRD patterns and (b) mass fractions of 20Ag/TiO₂ prepared at X/Y=8/5 (Fig. 2a) and annealed at 350 or 550 °C in air for 2 h. Diffraction patterns are marked for TiO₂ anatase (diamonds) and rutile (circles) and for Ag⁰ (squares), Ti₄O₇ (up triangles) and Ti₃O₅ (down triangles).

690, 765, 849 and 938 cm^{−1}) from amorphous Ti-suboxide [1] are not seen here. Chen et al. [1] suggested that their reduced TiO₂ phase was distorted, so, several titanium suboxide structures were present but could not be detected by XRD. Most importantly, when the Ag loading was increased from 10 to 20 wt.% in our samples and/or the flame conditions became more reducing (by increasing the precursor/fuel flow from 3 to 8 mL/min or changed the FSP feed ratio, X/Y, from 3/5 to 8/5), the anatase peaks at 514 and 639 cm^{−1} were broadened indicating distortion of the TiO₂ lattice [1,2].

The formation of “black” TiO₂ here is based on a different physical mechanism than wet-made “black” TiO₂ [1,2]: SMSIs between Ag⁰ and TiO₂ result in a crystalline suboxide (i.e. Ti₄O₇ and Ti₃O₅) that forms around the silver NPs on the TiO₂ support. As pointed out by Chen et al. [1], distortion of the reduced phases could be

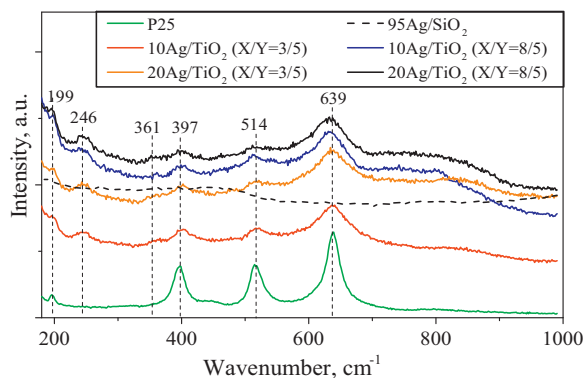


Fig. 4. Raman spectra of “black” TiO₂ NPs loaded with Ag (10 or 20 wt.%) and prepared at X/Y=3/5 or 8/5. For comparison, the Raman spectra of commercial TiO₂ (P25, Degussa) and FSP-made Ag (95 wt.%) supported on SiO₂ NPs (95Ag/SiO₂) are also included.

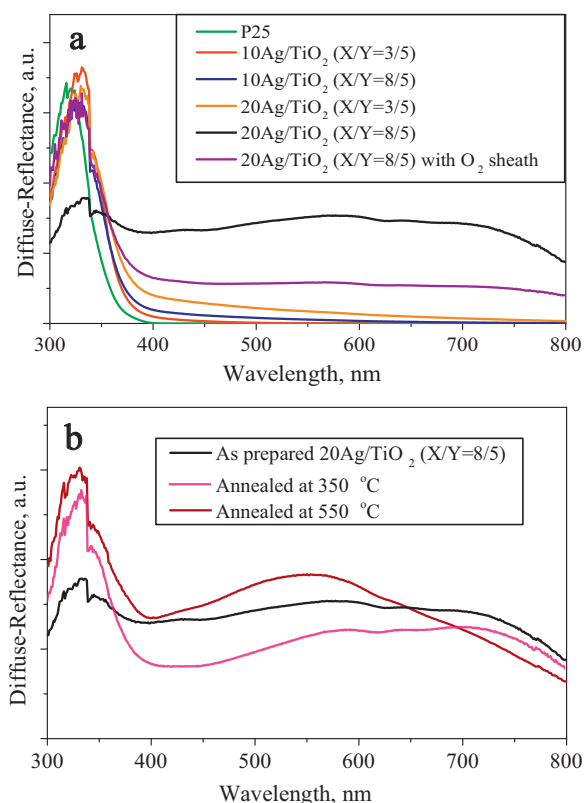


Fig. 5. Diffuse reflectance absorption spectra of (a) commercial TiO₂ (P25, green spectrum) and “black” TiO₂ NPs loaded with 10 and 20 wt.% Ag prepared at FSP feed ratios of X/Y = 3/5 and 8/5 in the absence or presence of 20 L/min sheath O₂ (red to purple spectra) (b) 20Ag/TiO₂ NPs “as prepared” at FSP feed ratio X/Y = 8/5 (black spectrum) and annealed at 350 °C (pink spectrum) or 550 °C (brown spectrum) in air for 2 h. (For interpretation of the references to colour in this figure legend, the reader is referred to the web version of the article.)

responsible for the distribution of the density of states creating the so-called energy tails that extend into the band-gap energies of the semiconductor. This phenomenon is responsible for light absorbance at visible wavelengths, rendering the black color of the as prepared Ag/TiO₂ NPs. Here the distorted phase of TiO_x is attributed to crystalline Ti₄O₇ and Ti₃O₅ as detected by XRD (Figs. 2a and 3a).

3.2. Visible light activity and photocatalysis

Fig. 5a shows UV–visible light absorption spectra of commercial TiO₂ (P25, green line) and various “black” TiO₂ (Fig. 1a) and 20Ag/TiO₂ prepared at FSP X/Y = 8/5 in the presence of 20 L/min O₂ sheath gas (from red to purple lines). The 20Ag/TiO₂ particles show significant absorption from 360 to 800 nm, which is the origin of their characteristic black color (Fig. 1a). However, the absorption band of Ag⁰ around 550 nm in the solid state [31] or 400 nm in the liquid phase [30] was not observed. Its absence is attributed to a strong electron interaction between Ag and Ti [32] induced by SMSI [9]. Thus, the improved light absorbance at visible wavelengths (400–800 nm) of all TiO_x/Ag/TiO₂ over commercial TiO₂ is attributed to the presence of TiO_x on the surface of the former.

Interestingly, “black” TiO₂ prepared at high Ag loading (20Ag/TiO₂) and high precursor concentration (X/Y = 8/5, black spectrum) exhibits greater absorption intensity in the visible range but lower in the UV than “black” TiO₂ prepared at more oxidative conditions, either at lower fuel concentration (X/Y = 3/5, orange spectrum) or with sheath O₂ (X/Y = 8/5, purple spectrum).

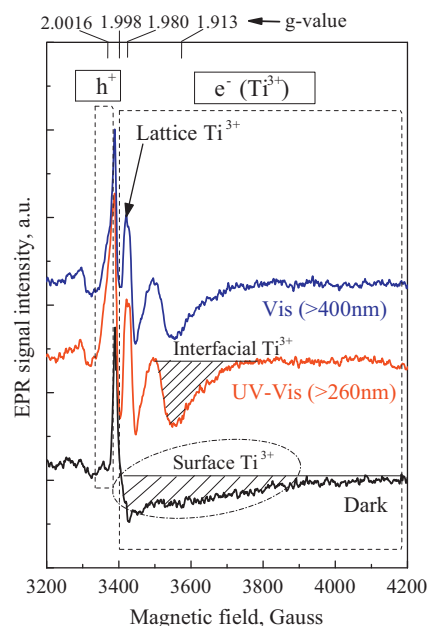


Fig. 6. Electron paramagnetic resonance (EPR) spectra for the 20Ag/TiO₂ NPs prepared at X/Y = 8/5 and recorded at 77 K in the dark (black; prior to illumination), after illumination with UV–vis radiation (red; $\lambda > 240$ nm), or vis radiation (blue; $\lambda > 400$ nm). (For interpretation of the references to colour in this figure legend, the reader is referred to the web version of the article.)

Fig. 5b shows the absorption spectra of 20Ag/TiO₂ NPs “as prepared” at X/Y = 8/5 (black spectrum) and annealed at 350 °C (pink spectrum) or 550 °C (brown spectrum) in air for 2 h. A 350 °C, the UV absorption of 20Ag/TiO₂ increases but in the visible decreases. Note that the mass fraction of the Ti-suboxides does not change (Figs. 2b and 3b). This indicates surface oxidation of TiO_x similar to 20Ag/TiO₂ NPs prepared at X/Y = 8/5 in the presence of sheath O₂ (Fig. 5a, purple spectrum). By annealing at 550 °C, the UV absorption further increases, compared to that at 350 °C as further conversion of suboxides and anatase to rutile took place (Fig. 3a). Furthermore, the plasmonic absorption of Ag around 550 nm [31] was revealed. This is attributed to removal of the Ti-suboxide (Fig. 3b, triangles at 550 °C) followed by Ag⁰ sintering and crystal growth (Fig. 3a).

Fig. 6 presents low-temperature EPR spectra (77 K) of 20Ag/TiO₂ prepared at X/Y = 8/5. In the dark (black line), the NPs contain two types of paramagnetic centers:

- (I) A sharp axial signal with $g = 1.998$ assigned to lattice electrons of anatase [33]. This g -component is attributed to the perpendicular g -tensor component of anatase Ti³⁺ bulk centers. Its sharp lineshape is characteristic of a well-defined local environment, which corresponds to Ti³⁺ centers localised inside the anatase nanocrystal. Thus both EPR and XRD show that the 20Ag/TiO₂ particles made at X/Y = 8/5 contain a well-ordered crystalline phase where Ti³⁺ centers are localised.
- (II) A broad signal extending from 3400 to 4000 Gauss corresponding to Ti³⁺ electron trapping sites [34]. Typically, surface Ti³⁺ electron trapping sites are characterized by EPR signals much broader than those in Fig. 6. Recently Naldoni et al. [35] showed that broad EPR signals from surface Ti³⁺ can be photoinduced in Pt-loaded TiO₂ or Au-loaded TiO₂ as in the case of P25 [33]. The narrower linewidth of the surface Ti³⁺ signals in Fig. 6 indicates restricted mobility of the trapped Ti³⁺ electrons; therefore, it is assigned to Ti³⁺ states localized at the interface of TiO₂. In parallel with the Ti³⁺ signals at $g < 2$, photoinduced h⁺ centers are detected under illumination at $g = 2.0016$ – 2.0024 [33].

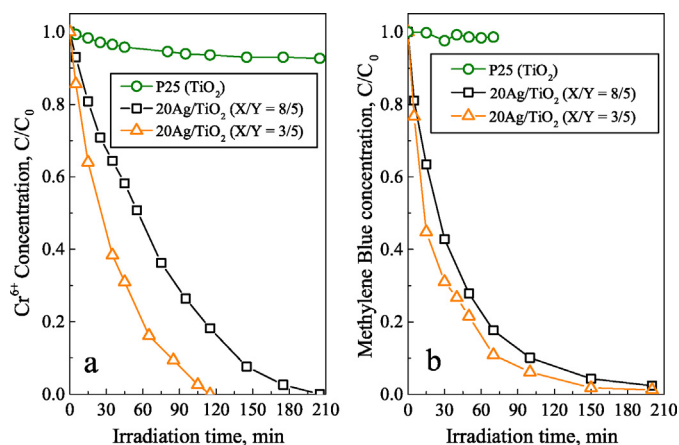


Fig. 7. Photocatalytic reduction of (a) Cr⁶⁺ ions and (b) methylene blue by pure TiO₂ (commercial P25, circles) and 20Ag/TiO₂ prepared by flame spray pyrolysis at X/Y = 3/5 (triangles) or 8/5 (squares) under visible-light irradiation (λ > 400 nm).

Titanium suboxides are rich in Ti³⁺ electron trapping sites which are easily detected by EPR spectroscopy [36]. In pure Ti₄O₇ or Ti₃O₅ crystals, the Ti³⁺ centers belong to lattice oxygen vacancies [28] of the type Ti³⁺–V_O–Ti⁴⁺. Here, the Ti³⁺ EPR signals are broader than Ti³⁺ in Ti₄O₇ indicating strain/distortion of the local environment around the Ti³⁺ centers. Irradiation under visible-light wavelengths (Fig. 6: blue line; λ > 400 nm) rapidly photoinduces (<30 s) three signals in Fig. 6: A strong narrow axial signal appears at g = 1.980 that is attributed to lattice electron (Ti³⁺) trapping sites at the interior of the crystal phase [33,34,37]. The broader trough-like signal at g = 1.913 is a characteristic of surficial electron-trapping Ti³⁺ sites [33]. Most importantly, the photogenerated e[−] and h⁺ signals can be induced at high yield (> 80%) under visible-light irradiation at λ > 400 nm (Fig. 6). This high visible-light photoactivity is consistent with the enhanced UV–vis absorbance (Fig. 5), which can be attributed to the generation of sub-band-gap energy tails from the distorted suboxide [1].

Plasmonic nanoparticles such as Ag⁰, Au⁰ attached on TiO₂ can enhance its photoactivity when excited at wavelengths matching their plasmonic resonance [38,39]. Here the plasmonic resonance peak of Ag is largely absent or weak in our Ag/TiO_x particles (Fig. 5) probably because of a strong electron interaction between Ag and Ti [32]. Thus the observed strong visible-light activity should originate primarily from the generation of sub-band-gap energy tails from the distorted suboxide, while the plasmonic contribution is minimal, if any. The absorption spectrum of Ag becomes strongly apparent after annealing at 550 °C for 2 h (Fig. 3a). Then Ag particles have sintered to 51 nm crystals and titanium suboxides have been fully oxidized.

Finally, Fig. 7a shows the visible-light photocatalytic activity of commercial TiO₂ (P25, circles) and present 20Ag/TiO₂ particles made at X/Y = 3/5 (triangles) and 8/5 (squares) for reduction of Cr⁶⁺, a priority toxic pollutant [20]. The half-life of Cr⁶⁺ was 30 and 55 min by 20Ag/TiO₂ NPs made at X/Y = 3/5 and 8/5, respectively. Furthermore, both photocatalysts are highly active also for methylene blue degradation under visible light irradiation with even shorter half lives of 15 and 25 min for the same NPs respectively (Fig. 7b). The faster kinetics of the NPs made at X/Y = 3/5 are consistent with their higher specific surface area (SSA) of 208 m²/g, which is almost twice that (113 m²/g) of the NPs made at X/Y = 8/5. In comparison, the P25 (reference TiO₂) exhibited the well known minor catalytic efficiency under visible light. Even though nanosilver on TiO₂ might slightly enhance the visible light photodegradation of phenol [40] and Alizarin Red S [41] by pure TiO₂ (P25), the present TiO₂/Ag/TiO_x nanostructures exhibit a much stronger photoactivity

due to suboxide presence [1,2]. This photoactivity is comparable to that of P25 for methylene blue under UV light.

4. Conclusions

Crystalline Ti-suboxide onto Ag nanoparticles supported on nanostructured titania exhibit strong photoactivity under visible light. These composite particles were made by scalable flame spray pyrolysis. Silver nanoparticles supported on TiO₂ catalyze the formation of crystalline titanium suboxides on the Ag/TiO₂ surface by strong metal–support interactions (SMSI) during their combustion synthesis as shown by microscopy, XRD, EPR and diffuse reflectance. These suboxides could be assigned to Ti₄O₇ and Ti₃O₅. Controlling their synthesis conditions provides an easy method to fine tune the composition of these “black” titania NPs and as a result, their photophysical and photocatalytic performance. Such heterostructural “black titania” is stable under ambient conditions and highly photoactive under UV and visible light as shown by EPR and rapid photodegradation of Cr⁶⁺ and methylene blue (down to 15 min half life for MB). As a result, these nanocomposite materials are attractive for photocatalytic and solar energy applications.

Acknowledgments

This research was supported in part by the Swiss National Science Foundation (grant no. 200021_149144) and the European Research Council under the European Union’s Seventh Framework Program (FP7/2007–2013, ERC grant agreement no. 247283).

References

- [1] X.B. Chen, L. Liu, P.Y. Yu, S.S. Mao, *Science* 331 (2011) 746–750.
- [2] A. Naldoni, M. Allietta, S. Santangelo, M. Marelli, F. Fabbri, S. Cappelli, C.L. Bianchi, R. Psaro, V. Dal Santo, *J. Am. Chem. Soc.* 134 (2012) 7600–7603.
- [3] C. Langlade, B. Vannes, T. Sarnet, M. Autric, *Appl. Surf. Sci.* 186 (2002) 145–149.
- [4] F. Zuo, L. Wang, T. Wu, Z. Zhang, D. Borchardt, P. Feng, *J. Am. Chem. Soc.* 132 (2010) 11856–11857.
- [5] S. Tominaka, *Chem. Commun.* 48 (2012) 7949–7951.
- [6] S. Tominaka, *Inorg. Chem.* 51 (2012) 10136–10140.
- [7] H.M. Liu, W.S. Yang, Y. Ma, J.N. Yao, *Appl. Catal. A: Gen.* 299 (2006) 218–223.
- [8] S.J. Tauster, *Acc. Chem. Res.* 20 (1987) 389–394.
- [9] S.J. Tauster, S.C. Fung, R.T.K. Baker, J.A. Horsley, *Science* 211 (1981) 1121–1125.
- [10] R.T.K. Baker, E.B. Prestridge, L.L. Murrell, *J. Catal.* 79 (1983) 348–358.
- [11] S.J. Tauster, S.C. Fung, R.L. Garten, *J. Am. Chem. Soc.* 100 (1978) 170–175.
- [12] A.R. Gonzalez-Elipio, J. Soria, G. Munuera, *J. Catal.* 76 (1982) 254–264.
- [13] S.C. Fung, *J. Catal.* 76 (1982) 225–230.
- [14] J. Sa, J. Bernardi, J.A. Anderson, *Catal. Lett.* 114 (2007) 91–95.
- [15] R.T.K. Baker, E.B. Prestridge, R.L. Garten, *J. Catal.* 56 (1979) 390–406.
- [16] R. Strobel, S.E. Pratsinis, *J. Mater. Chem.* 17 (2007) 4743–4756.
- [17] R. Mueller, L. Madler, S.E. Pratsinis, *Chem. Eng. Sci.* 58 (2003) 1969–1976.
- [18] S.E. Pratsinis, *AIChE J.* 56 (2010) 3028–3035.
- [19] L. Madler, W. Stark, S.E. Pratsinis, *J. Mater. Res.* 18 (2003) 115–120.
- [20] M.R. Prairie, L.R. Evans, B.M. Stange, S.L. Martinez, *Environ. Sci. Technol.* 27 (1993) 1776–1782.
- [21] A. Houas, H. Lachheb, M. Ksibi, E. Elaloui, C. Guillard, J.M. Herrmann, *Appl. Catal. B: Environ.* 31 (2001) 145–157.
- [22] V.R. Porter, W.B. White, R. Roy, *J. Solid State Chem.* 4 (1972) 250–254.
- [23] V.A. de la Pena O’Shea, M.C. Alvarez Galvan, A.E. Platero Prats, J.M. Campos-Martin, J.L.G. Fierro, *Chem. Commun.* 47 (2011) 7131–7133.
- [24] R.T.K. Baker, E.B. Prestridge, R.L. Garten, *J. Catal.* 59 (1979) 293–302.
- [25] D.R. Ou, T. Mori, H. Togasaki, M. Takahashi, F. Ye, J. Drennan, *Langmuir* 27 (2011) 3859–3866.
- [26] S.E. Pratsinis, *Prog. Energy Combust. Sci.* 24 (1998) 197–219.
- [27] S. Tominaka, H. Yoshikawa, Y. Matsushita, A.K. Cheetham, *Mater. Horizons* 1 (2014) 106–110.
- [28] D. Goldschmidt, M. Watanabe, *Mater. Res. Bull.* 20 (1985) 65–70.
- [29] A. Teleki, S.E. Pratsinis, *PCCP* 11 (2009) 3742–3747.
- [30] G.A. Sotiropoulos, S.E. Pratsinis, *Environ. Sci. Technol.* 44 (2010) 5649–5654.
- [31] C. Gunawan, W.Y. Teoh, C.P. Marquis, J. Liffa, R. Amal, *Small* 5 (2009) 341–344.
- [32] I. Honma, T. Sano, H. Komiyama, *J. Phys. Chem.* 97 (1993) 6692–6695.
- [33] Y. Nakaoka, Y. Nosaka, *J. Photochem. Photobiol. A* 110 (1997) 299–305.
- [34] T. Rajh, A.E. Ostafin, O.I. Micic, D.M. Tiede, M.C. Thurnauer, *J. Phys. Chem.* 100 (1996) 4538–4545.
- [35] A. Naldoni, M. D’Arienzo, M. Altomare, M. Marelli, R. Scotti, F. Morazzoni, E. Selli, V. Dal Santo, *Appl. Catal. B: Environ.* 130–131 (2013) 239–248.

- [36] J.F. Houlihan, L.N. Mulay, *Mater. Res. Bull.* 6 (1971) 737–742.
- [37] D.C. Hurum, K.A. Gray, T. Rajh, M.C. Thurnauer, *J. Phys. Chem. B* 109 (2005) 977–980.
- [38] C. Gomes Silva, R. Juárez, T. Marino, R. Molinari, H. García, *J. Am. Chem. Soc.* 133 (2010) 595–602.
- [39] D. Tsukamoto, Y. Shiraishi, Y. Sugano, S. Ichikawa, S. Tanaka, T. Hirai, *J. Am. Chem. Soc.* 134 (2012) 6309–6315.
- [40] E. Grabowska, A. Zaleska, S. Sorgues, M. Kunst, A. Etcheberry, C. Colbeau-Justin, H. Remita, *J. Phys. Chem. C* 117 (2013) 1955–1962.
- [41] M.L. de Souza, P. Corio, *Appl. Catal. B: Environ.* 136 (2013) 325–333.